Research Article Vol. 63, No. 21 / 20 July 2024 / Applied Optics 5699

applied optics

Wavelength-tolerant generation of Bessel-Gaussian beams using vortex phase plates

Lyubomir Stoyanov,[1,2] Nikolay Dimitrov,[1] Felix Wiesner,[2,3] Michael Fedoruk,[4] Gerhard G. Paulus,[2,3] and Alexander Dreischuh[1,*]

[1]Department of Quantum Electronics, Faculty of Physics, Sofia University, 5, J. Bourchier Blvd., Sofia-1164, Bulgaria
[2]Institute of Optics and Quantum Electronics, Friedrich Schiller University, Max-Wien-Platz 1, D-07743 Jena, Germany
[3]Helmholtz Institute Jena, Helmholtzweg 4, D-07743 Jena, Germany
[4]Vortex Photonics, Hubertusstr. 11, D-82152 Planegg, Germany
*ald@phys.uni-sofia.bg

Received 21 March 2024; revised 12 June 2024; accepted 1 July 2024; posted 1 July 2024; published 17 July 2024

With their nearly non-diffracting and self-healing nature, Bessel-Gaussian beams (BGBs) are attractive for many applications ranging from free-space communications to nonlinear optics. BGBs can successfully be generated on background laser beams by imprinting and subsequently annihilating multiply charged optical vortices followed by focusing the resulting ring-shaped beam with a thin lens. For high-power applications optical vortices are preferentially created by spiral phase plates because of their high damage threshold. These are fabricated to realize an azimuthal change of the accumulated phase of a multiple of 2π at a predetermined wavelength. This raises the expectation that the use of spiral phase plates for the generation of BGBs is limited to the design wavelength and therefore not applicable to broadband applications involving short-pulse lasers. In this paper we present experimental data showing that this limitation can be overcome in a broad spectral range around the design wavelength. Experimental cross-sections of the BGBs for several off-design wavelengths are found in a good quantitative agreement with the theoretical Bessel functions at distances up to 540 cm after the focus of the lens.

https://doi.org/10.1364/AO.524178

1. INTRODUCTION

Together with the infinite plane waves, Airy, and Ince beams, Bessel beams belong to the four known types of beams that are exact solutions of the Helmholtz equation [1,2]. Qualitatively described, the intensity distribution of a Bessel beam (BB) consists of a central peak (for a zeroth-order BB) or a central ring (for first- and higher-order BBs), which, in the strict mathematical sense, is surrounded by an infinite number of coaxial rings [1,3] of decreasing amplitudes in radial direction. The minima between the rings are at zero intensity since the phase of the BB contains π-phase jumps in radial direction [3]. The BBs are designated as non-diffracting in the sense of the remarkable stability of the central peak (or the central ring) with respect to diffraction broadening [4]. Naturally, the exact experimental realization of BBs is not possible since every laser beam has a finite transverse size in reality. Thus, the central peak of an experimentally obtained BB is surrounded by a finite number of coaxial rings. As a consequence, such BBs exhibit a weakly pronounced divergence and thus are referred to as quasi-non-diffracting Bessel-Gaussian beams (BGBs).

Some of the classical and well-studied methods for the generation of BGBs use either annular slits in the back focal plane of a lens [4–6], or axicons [4], or devices reproducing the phase structure of axicons such as deformable mirrors [7], spatial light modulators [8], or computer-generated holograms [9]. Another interesting method is the use of a cylindrical lens morphed to a closed ring [10]. The problem with some of these methods is the relatively poor approximations of BBs or the low efficiency in the conversion of the Gauss beam into a BGB. Both can be overcome by an approach based on the manipulation of highly charged optical vortices (OVs) [11–13].

OVs are doughnut-shaped beams carrying truly two-dimensional point phase dislocation in their dark cores [14]. Their phase profiles are described by integers (with signs) known as topological charges (TCs), which indicate the number of 2π-unit phase windings in azimuthal direction. Generally, the higher the TC of an OV, the broader the dark core of the OV beam (see, e.g., Fig. 2(b) in [11]) and the more unstable the multiply charged vortex state [15,16]. In other words, highly charged OVs can be used to efficiently generate a ring-shaped intensity distribution as required for producing a BGB. Of course, the phase singularities in this ring-shaped beam need to be removed, which is accomplished by using an identical optical element with an encoded opposite TC. The Fourier-transform of the resulting beam by a thin lens results in a BGB in and after the lens' focus. It has been shown [11–13] that such BGBs can

propagate for meters with half-angle divergences on the order of a few tens of microradians and with a quality exceeding those of BGBs generated with axicons.

In [11–13] reflective liquid-crystal spatial phase modulators (SLMs), programmed to reproduce the phases of the desired multiply charged OVs, are used. Unfortunately, despite their high efficiency, these SLMs cannot withstand high average and high peak powers. A possible alternative would be the use of vortex phase plates (VPs), i.e., plates whose thickness increases in azimuthal direction [17,18]. Such plates are designed and produced for a given wavelength to provide an azimuthal phase change of an integer multiple of 2π. Their use at other wavelengths leads to the generation of optical vortices with fractional TCs (see, e.g., Figs. 3(c), (d) in [19], Fig. 2 in [20], and Fig. 4 in [21]). These perturbed vortices are accompanied by radial modulations of the amplitude of the background beam. Even though the idea for an achromatic phase plate, i.e., for compensating for the topological dispersion by a two-layered OV phase plate, is known [22], we are not aware of its experimental implementation.

The purpose of this paper is to report experimental results for the successful generation of long-range low-divergent BGBs by using transmissive vortex phase plates at wavelengths substantially different from their design wavelength. This allows us to specify the discussed method as wavelength-tolerant or insensitive to topological dispersion. The use of two identical transmissive VPs is simple and allows obtaining first-order BGB as well. The demonstrated approach works even with a single transmissive VP aligned in a double-pass configuration. Noteworthy is the plainness of both experimental realizations. The results can be especially important for, e.g., applications using ultrashort broadband pulses.

2. EXPERIMENTAL ARRANGEMENTS

In this section, the experimental setups are presented in details. The first, single-pass experimental setup [see Fig. 1(a)] assumes the presence of two identical uncoated VPs (VP1 and VP2; both designed for $|TC| = 32$ at 532 nm) with one of them being flipped with respect to the other. This allows generating zeroth-order BGB. In order to generate first-order BGB, a third VP3 with $|TC| = 1$ is added. Alternatively, two highly charged VPs with a difference of ± 1 of the TC can be used in a sequence as VP1 and VP2. In our case, the uncoated VP3 is designed to produce an OV with $|TC| = 1$ at a wavelength of 800 nm. A focusing lens L with $f = 125$ mm is used as a Fourier-transforming element in space. The generated Bessel-Gaussian beams are recorded by a CCD camera at distances up to 300 cm behind the focus of the lens L. To show the wavelength tolerance of the used method for BGB generation we used a laser system tunable from 420 nm to 800 nm. The used power in this experiment was in the mW range, although the VPs can withstand much higher powers/intensities. Figs. 1(c) and 1(d) show experimental intensity distributions generated at 800 nm at a propagation distance of 100 cm of zeroth-order BGB (obtained with VP1 and VP2 designed for 532 nm) and first-order BGB (obtained in the same way plus VP3 designed for 800 nm). The intentionally saturated frames clearly show the good quality of the rings surrounding the central peak/ring of the BGBs.

The second variant of the setup is shown in Fig. 1(b). It uses a double-pass through a single (highly charged) transmissive uncoated VP, thus allowing the generation of zeroth-order BGBs. Laser beams of different wavelengths (455 nm, 532 nm, 633 nm, and 800 nm) are used for this experiment. For reasons of experimental convenience, the laser is fed in via a multimode optical fiber (OF) with beam collimation optics. Here, only VP1 is used ($|TC| = 32$ at 532 nm). After passing through a focusing lens L ($f = 125$ mm), the ring-shaped vortex beam is reflected from two flat mirrors M1 and M2. Accordingly, the TC is erased after the second pass through the backside of the VP1. The lens L has two functions, namely, to compensate for the diffraction of the ring-shaped beam reflected from mirrors M1 and M2 at the position of the VP1, and to Fourier-transform it. The Bessel-Gaussian beams are recorded at distances up to 540 cm behind the focus of the lens L by translating a charge-coupled device camera.

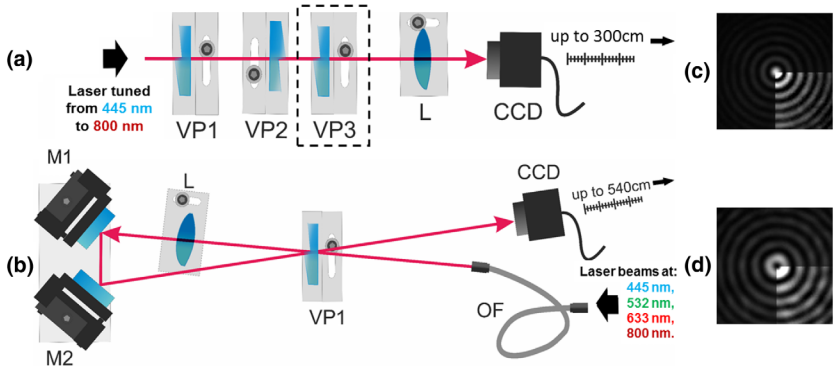

Fig. 1. Experimental setup. (a) Single-pass configuration: the tunable laser beam illuminates a sequence of VPs. VP1 and VP2 are designed for 532 nm with $|TC| = 32$ and are oriented to cancel the overall TC. VP3 (optional) is designed for 800 nm with $|TC| = 1$. VP1-to-VP2 separation – 5 cm, VP2-to-VP3 distance −5 cm. (b) Double-pass configuration: a laser beam from one of the four laser sources is transmitted through a multimode optical fiber (OF) and illuminates VP1. M1 and M2 – flat silver-coated mirrors. The Bessel-Gaussian beams are recorded at various distances by a CCD camera. The same focusing lens (L; $f = 125$ mm) and CCD camera are used in both setups. (c) (d) Zeroth- and first-order Bessel-Gaussian beams at 800 nm using the single-pass setup, recorded at 100 cm behind the focus of the lens L.

3. RESULTS AND DISCUSSION

In order to demonstrate the remarkable robustness of the vortex method for producing BGBs against the use of the "wrong" wavelength, we start with a few measurements that illustrate the difference between OVs generated at the wavelength for which the corresponding VP is designed and the (fractional) OVs when the same VP is illuminated at significantly different wavelengths. When the OVs are produced with VPs illuminated at the design wavelengths, OVs with integer TCs are generated. The corresponding frames are shown in Fig. 2(a) enclosed by a dashed line. What can be seen in the upper dashed panel of Fig. 2(a) is the good quality of the OV with $|TC| = 1$ generated at the "correct" wavelength $\lambda_C = 532$ nm. At the "wrong" wavelengths ($\lambda_1 = 633$ nm $\approx \lambda_C \times 1.19$ and $\lambda_2 = 800$ nm $\approx \lambda_C \times 1.5$), optical vortices with fractional topological charges are generated. The fact that the phase spirals are not up to 2π (or multiples) leads, immediately after the VP, to additional radial dark structures. Such structures are clearly seen in the upper middle and right frames of Fig. 2(a) for $|TC| = 1$ for the "wrong" wavelengths.

In the first line of frames in Fig. 2(a), in each of the three intensity distributions of OVs with $|TC| = 1$, we showed as insets the essential portions of the corresponding interference patterns obtained with a tilted plane wave. The interferogram recorded at a wavelength of 532 nm clearly shows a splitting of one interference line into two, which is the expected indication of a unit topological charge. Away from the vortex core in a vertical direction, the interference lines remain nearly straight and undisturbed by the weak intensity modulation of the background beam carrying the vortex.

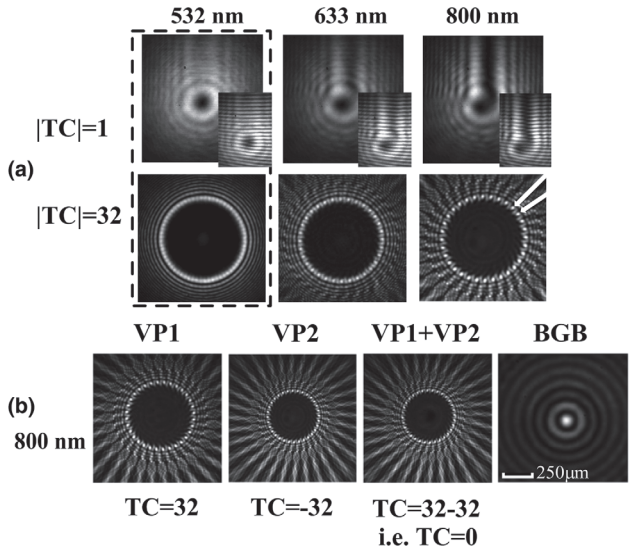

Fig. 2. Near-field results – 5 cm after the last illuminated VP. (a) Demonstration of OVs with integer TCs (dashed rectangle: at the "correct" wavelength) and with fractional TCs. Results obtained by laser beams at 532 nm, 633 nm, and 800 nm transmitted through VP designed for $|TC| = 1$ (upper row) and $|TC| = 32$ (lower row) at a wavelength of 532 nm. For each OV intensity distribution with $|TC| = 1$, as insets we also include parts of the corresponding interference patterns (see text for more details). (b) OVs recorded using the single-pass setup (see Fig. 1), when VP1 with encoded $TC = 32$ is aligned only (first frame), when only VP2 with encoded $TC = -32$ is present (second frame), and when both VP1 and VP2 are aligned so that all TCs are erased (third frame; effectively $TC = 0$). VP1 and VP2 are designed for a wavelength 532 nm and are illuminated with a laser beam at 800 nm. Rightmost frame: BGB obtained by focusing the ring-shaped beam shown on the third frame, 100 cm behind the focus of the lens L ($f = 125$ mm).

In the interferograms taken at wavelengths 633 nm and 800 nm the change is significant. In both cases, a relatively well-formed optical vortex with a unit topological charge remains in the center of the background beam and a well-defined fork-like splitting of one interference line into two is observed. In the vertical radial direction, however, one-dimensional dark beams are visible. Their modulation depth increases with increasing the offset from the design wavelength of the vortex plate. At a wavelength of 633 nm, the interference lines are slightly bent, indicating a slight phase change in the dark beam. At a wavelength of 800 nm, especially in the region closer to the OV core, interference fringes shifted by half a period are clearly visible. This is an indication of a one-dimensional phase dislocation, which can also be interpreted as a sequence of closely spaced OVs with alternative single topological charges $+1-1+1\ldots$ etc. The bending of the dark structure near the well-formed OV with a unit topological charge is a consequence of the linear dynamics of the beam under the influence of the diffraction (see, e.g., Fig. 2 in [20], however numerically calculated in a nonlinear regime). In view of the above, one can state that at wavelengths significantly different from the design wavelength of the used vortex plate, OVs with fractional topological charges are formed.

In general, multiply charged optical vortices decay into vortices with unit topological charges of the same signs. Due to their mutual repulsion, broad bright ring-shaped beams are formed. In the three lower panels of Fig. 2(a) we compare OVs with $|TC| = 32$ obtained when laser beams at 532 nm, 633 nm, and 800 nm are transmitted through a VP designed for 532 nm. At the "correct" wavelength, the dominating inner bright ring is surrounded by rings of rapidly decreasing intensities. This is a clear signature of diffraction accumulated by the ring-shaped beam after the VP. These rings are well formed and smooth in azimuthal direction. This is definitely not the case at the offset wavelengths of 633 nm and 800 nm. In these cases, the rings surrounding the dark core are periodically modulated in azimuthal direction. Close inspection of the results shows that the number of the modulation periods is equal to the encoded integer TC for the "correct" wavelength.

We also consider it important to present the near-field (5 cm after the last illuminated VP) energy density distributions of the optical vortices and the annihilated ring-shaped beam generated at 800 nm from VPs designed to produce an optical vortex with topological charge 32 at 532 nm [Fig. 2(b)]. This case corresponds to the single-pass setup described in Fig. 1(a). The transverse intensity distributions of the OVs are recorded when only VP1 encoded with $TC = 32$ is used (left frame), only in the presence of VP2 encoded with $TC = -32$ (second frame) and when both VP1 and VP2 are aligned and all TCs are erased (third frame). An inversion of the sign of the TC is achieved by flipping one of the VPs, i.e., by illuminating it from the back side. The ring-shaped beam obtained by VP2 only, has a smaller radius than the one obtained by using VP1 only, since VP2 is located closer to the CCD camera. The panel marked as

VP1 + VP2 denotes the result when both VPs are aligned and all TCs are erased (final TC = 32 − 32 = 0). The interesting thing to note here is that, despite the absence of phase singularities inside the ring-shaped beam, the intensity distribution remains similar to the one generated with VP2 only. This is in agreement with the results reported in [11,12]. Even such strongly perturbed ring-shaped beams at "wrong" wavelengths result in high-quality BGBs after Fourier-transformation in space. One such BGB is shown in the most right frame of Fig. 2(b). It is obtained by focusing the beam shown in the third panel in Fig. 2(b). The presented BGB is captured 100 cm after the focus of the Fourier-transforming lens.

Figure 3 shows a set of graphs representing experimental data obtained with the single-pass experimental setup [see Fig. 1(a)]. Each graph contains the experimentally recorded radial profile of the zeroth-order BGB (hollow colored circles) and a numerically generated radial profile of a perfect (in the mathematical sense) Bessel (colored solid curves). For the numerical generation of Bessel functions to approximate the experimental data we used the Hansen-Bessel formula [23]

$$I_n(\rho r) = \frac{1}{4\pi^2}\left|\int_{-\pi}^{\pi} \exp\left(-i\rho\cos(\theta)r - in\theta\right) \mathrm{d}\theta\right|^2. \quad (1)$$

In this equation ρ (the length of the transverse component of the wave-vector) was the only parameter to be adjusted, θ is the

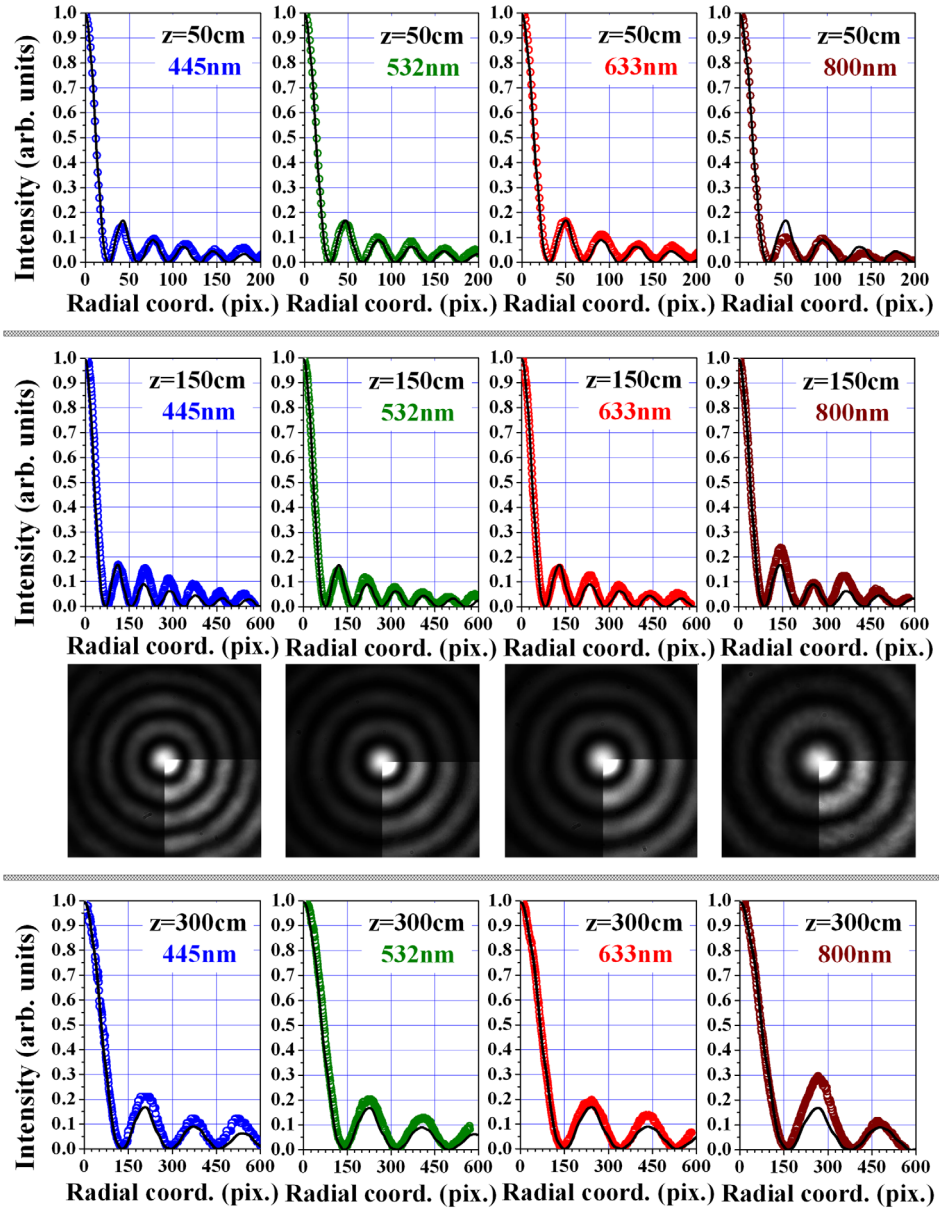

Fig. 3. BGBs generated using the single-pass setup shown in Fig. 1(a). Graphs: radial cross-sections of experimentally generated BGBs (open circles) and their numerical approximations with Bessel functions [solid curves; see Eq. (1)] at propagation distances 50 cm (first row), 150 cm (second row), and 300 cm (bottom row) and at different wavelengths (445 nm, 532 nm, 633 nm, and 800 nm) as indicated by the respective labels. The intensity distributions in the third row display the intensity profiles of the BGBs at a distance of 150 cm. For better visibility, one quarter of each frame is raised in brightness and contrast.

azimuthal angle, r is the transverse coordinate, and $n = 0$, 1 for zeroth- or first-order Bessel functions, respectively.

The specific distances at which the data are presented (50 cm, 150 cm, and 300 cm) and the laser wavelengths used in each case are denoted in each plot. (More experimental cases for different wavelengths are summarized in Supplement 1 to this paper.) The intensity distributions shown in the third row are experimentally recorded BGBs from which the respective radial profiles at 150 cm are extracted. For better visibility, one quarter of each frame is intensified in brightness and contrast. Generally one can state that the agreement between experimental data and numerical approximations is excellent.

Let us analyze the results in more detail. The second column of graphs represents the case of "correct" use of the pair of VPs. The excellent agreement between the experimental and numerical data in this case can be regarded as a reference when evaluating the other three cases. Remarkably, the theoretical and experimental data agree virtually as well for the "wrong" wavelengths. The only noticeable difference is observed at a wavelength of 800 nm, which may be expected as this wavelength differs most (270 nm) from the design wavelength. The deviations are in the relative intensities of the outer-lying bright rings, not in their relative positions. Nonetheless, the wavelength-tolerant performance of the setup is confirmed and high-quality BGBs are generated. At the longest propagation distance after the focal plane of the lens (300 cm in this experiment), in all four cases the experimental intensities of the satellite rings are slightly higher than the theoretical ones. However, the deduced divergences (half-angles) of the obtained BGBs are 108 μrad for 445 nm, 126 μrad for 532 nm, 122 μrad for 633 nm, and 128 μrad for 800 nm, in agreement with the values obtained in previously published works [11–13]. No significant change of the overall efficiency is measured when generating BGBs at the "wrong" wavelengths using uncoated VPs.

In Fig. 4 we show a comparison of the transverse profiles of the BGBs followed up to 540 cm, obtained at the "correct" wavelength [532 nm; Fig. 4(a)] and at one "wrong wavelength" of 800 nm [Fig. 4(b)]. Qualitatively, they are very similar. The only weakly pronounced difference is that at the end of the propagation range the outer-lying satellite rings of the BGB obtained at 800 nm are slightly more visible compared to the corresponding rings at 532 nm. This is quantitatively confirmed when inspecting the graph shown in Fig. 4 (right panel) and agrees with the results shown in the lowest row of Fig. 3 for 532 nm and 800 nm.

The data presented in Fig. 5 are recorded at 633 nm and 700 nm, using the single-pass setup again. They are intentionally chosen to significantly deviate from both design wavelengths for VP1, VP2 (532 nm), and VP3 (800 nm). Remarkable is that at both wavelengths, the cores of the OVs carried by the central rings of the first-order BGBs are well formed and modulated down to zero. For both wavelengths, the radial profiles at 150 cm agree equally well with the numerical ones. The measured angles of divergence corresponding to the profiles shown in Fig. 5 are 140 μrad for both 633 nm and 700 nm.

Another interesting observation in these experiments is the increase of the ring's azimuthal modulation when using wavelengths closer to the blue part of the spectrum. This can be

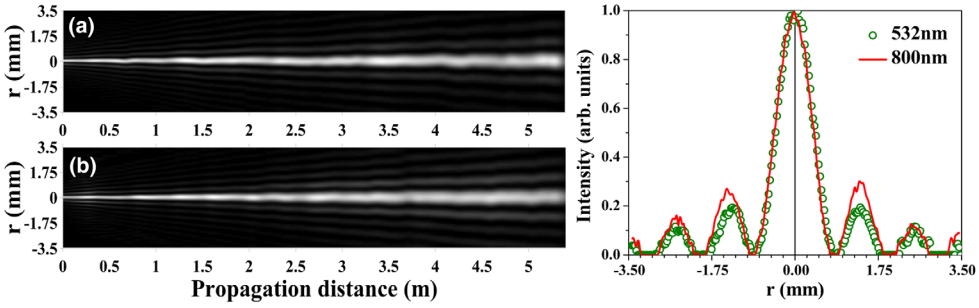

Fig. 4. Longitudinal intensity distributions of the diametrical cross-sections of the BGBs generated at (a) 532 nm and (b) 800 nm up to 540 cm with the single-pass configuration [see Fig. 1(a)]. Graph: comparison of the normalized diametrical intensity distributions of the two BGBs shown in (a) and (b). The corresponding experimental frames from which the data for the graph are extracted are captured at a propagation distance of 540 cm.

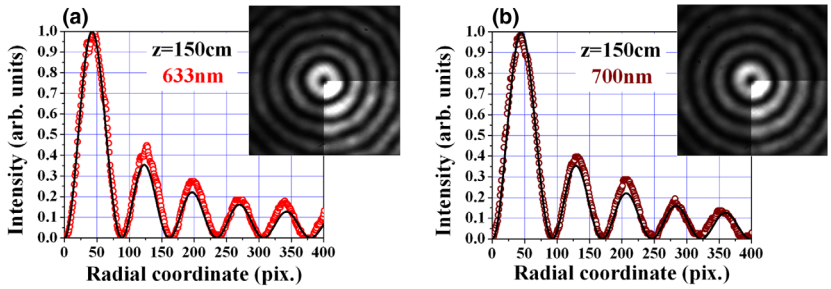

Fig. 5. First-order BGBs generated using the single-pass setup [shown in Fig. 1(a)] at wavelengths 633 nm (left) and 700 nm (right). The radial cross-sections of the generated BGBs (open circles) and their numerical approximations with Bessel functions (solid curves) are recorded 150 cm after the lens. VP1 and VP2 are designed for 532 nm with $|TC| = 32$. VP3 is designed for 800 nm with $|TC| = 1$. All VP design wavelengths differ significantly from those used in the experiment.

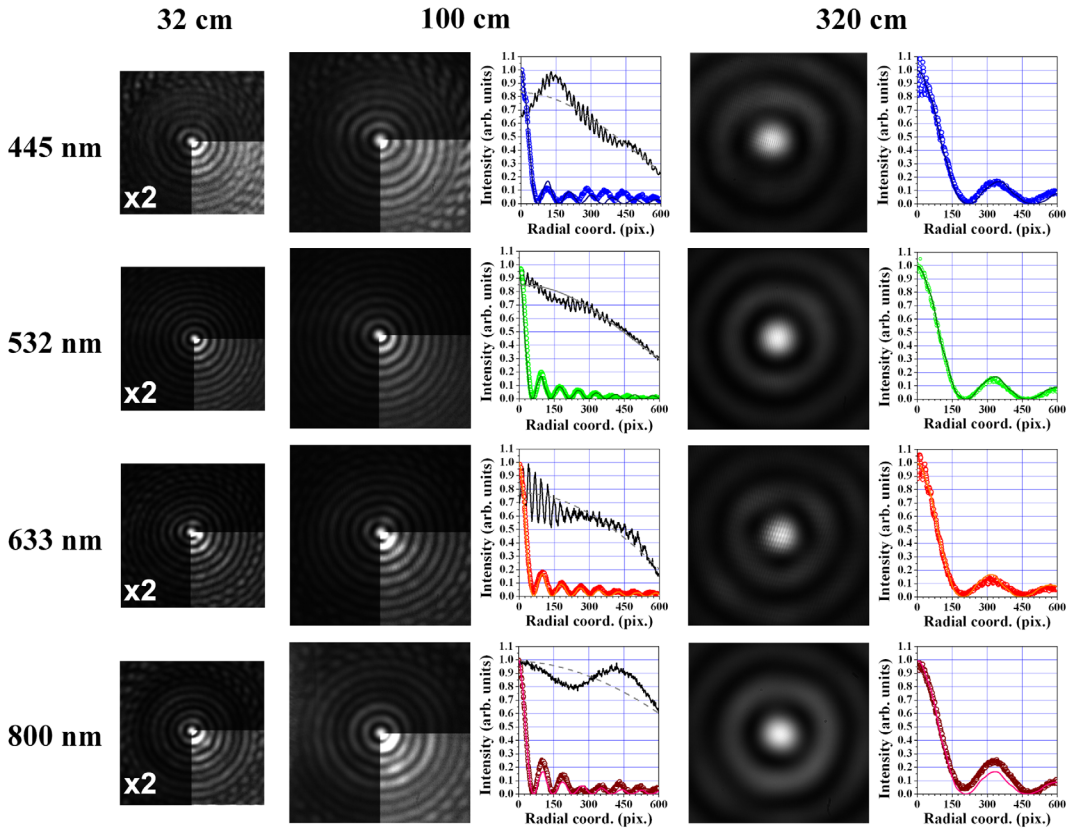

Fig. 6. Two-dimensional intensity distributions and radial cross-sections of BGBs generated using the double-pass setup shown in Fig. 1(b) at four different wavelengths, captured at 32 cm, 100 cm, and 320 cm after the vortex plate. Design wavelength of the used VP is 532 nm. One quarter of the intensity distributions at 32 cm and 100 cm are raised in brightness and contrast for better recognition of the outer-lying rings surrounding the bright central peak.

explained by the increasing deviation of the used wavelength from the design wavelength of VP3 (800 nm). It should be kept in mind that VP3 is generating a singly charged OV at the "correct" wavelength but a fractional vortex at the "wrong" wavelengths, almost doubling its TC when approaching 400 nm. As expected, such modulations are absent at 800 nm.

In Fig. 6 we summarize the intensity distributions of the BGBs obtained using the described double-pass setup [Fig. 1(b)] with a VP designed for $|TC| = 32$ at 532 nm. The data is captured at four different wavelengths and at distances of 32 cm, 100 cm, and 320 cm after the vortex plate. At 100 cm and 320 cm we also show the corresponding experimental radial cross-sections (open circles) and their numerical approximations with Bessel functions (solid curves). The graphs for propagation distances 100 cm present also the beam profiles when the VP is removed from the setup (see the black curves in the upper part of the graphs). They exhibit fairly strong modulations caused by the multi-mode fiber delivering the different laser beams to the entrance of the double-pass setup [Fig. 1(b)]. The gray dashed curves are the corresponding parabolic approximations of the beam, included to guide the eye only. In consideration of the highly irregular input beam, the clean profiles of the generated BGBs are particularly noteworthy.

Careful inspection of the frames shows once again (e.g., for 32 cm and for 100 cm) that the quality of the rings surrounding the central peak of the zeroth-order BGBs is the best for the wavelength for which the plates are designed (532 nm). At the "wrong" wavelengths, the residual modulation caused mostly by the vortices with fractional topological charges, is probably positively influenced by the self-healing nature of the BGBs.

Generally speaking, given the significant offsets of the wavelengths from the design wavelength ($\lambda_{min} = 445$ nm $\approx \lambda_C \times 0.84$ and $\lambda_{max} = 800$ nm $\approx \lambda_C \times 1.5$) the results can be characterized as surprisingly good. The latter is also confirmed by the data for the divergences of the central peaks of the beams. The estimated divergences for the zeroth-order BGBs are 164 μrad at 800 nm, 136 μrad at 633 nm, 150 μrad at 532 nm, and 165 μrad and 445 nm. [We attribute the slightly larger values compared to those measured in our previous works [11,12] to the significantly shorter focal length of the Fourier-transform lens used here ($f = 125$ mm)]. The two lowest values of the divergences are for 532 nm and 633 nm. Again, only for the case of 800 nm (the largest offset from the design wavelength), there are weak deviations of the experimental results from the numerical approximations.

4. CONCLUSION

High-quality long-range Bessel-Gaussian beams can be generated by annihilating highly charged OVs using vortex phase plates even at wavelengths significantly different from the design

wavelength of the vortex plates. This has been confirmed for two completely different experimental schemes, namely, for a single-pass and a double-pass configuration. The plainness of the approach is noteworthy. In the simplest case, only one vortex plate is necessary for BGB generation and its design wavelength does not even play a major role. Furthermore, the beam quality of the used lasers is proved to have minimal effect on the obtained BGB. Further sets of experimental data confirming these statements are presented in Supplement 1 to this paper. Obviously, these properties make high-power, high-quality, long-range Bessel-Gaussian beams more easily accessible for any laser laboratory. Moreover, the robustness of the approach against wavelength mismatch suggests the applicability for few-cycle pulses [13]. We believe that the long-range low-divergence Bessel-Gaussian beams generated by the described method can add one new degree of freedom to, e.g., the orbital angular momentum multiplexing with BGBs [24,25]—namely, the possibility to realize an analog of the wavelength-division multiplexing and beam propagation in free space based on this wavelength- and intensity-tolerant scheme for BGB generation.

Funding. Bulgarian National Science Fund (КП-06-ПН78/12); Ministry of Education and Science (ELI-ERIC-BG, National Roadmap for Scientific Infrastructure); Ministry of Education and Science (BG-RRP-2.004-0008-C0); Deutsche Forschungsgemeinschaft (PA 730/13).

Acknowledgment. We acknowledge the support provided by the National Roadmap for Scientific Infrastructure, financially coordinated by the Ministry of Education and Science of the Republic of Bulgaria. The work of L.S., N.D., and A.D. was also supported by the European Union-NextGenerationEU, through the "National Recovery and Resilience Plan of the Republic of Bulgaria". L.S. would like to gratefully acknowledge the Return Grant awarded by the Alexander von Humboldt Foundation. F.W. is part of the Max Planck School of Photonics supported by BMBF, the Max Planck Society, and the Fraunhofer Society.

Disclosures. The authors declare no conflicts of interest.

Data availability. The datasets generated and analyzed during the current study are available from the corresponding author upon reasonable request.

Supplemental document. See Supplement 1 for supporting content.

REFERENCES

1. J. Durnin, "Exact solutions for nondiffracting beams. I. The scalar theory," J. Opt. Soc. Am. A **4**, 651–654 (1987).
2. S. N. Khonina, A. V. Ustinov, and S. Chávez-Cerda, "Generalized parabolic nondiffracting beams of two orders," J. Opt. Soc. Am. A **35**, 1511–1517 (2018).
3. Y. Lin, W. Seka, J. H. Eberly, *et al.*, "Experimental investigation of Bessel beam characteristics," Appl. Opt. **31**, 2708–2713 (1992).
4. D. McGloin and K. Dholakia, "Bessel beams: diffraction in a new light," Contemp. Phys. **46**, 15–28 (2005).
5. J. Durnin, J. J. Miceli, and J. H. Eberly, "Diffraction-free beams," Phys. Rev. Lett. **58**, 1499–1501 (1987).
6. G. Indebetouw, "Nondiffracting optical fields: some remarks on their analysis and synthesis," J. Opt. Soc. Am. A **6**, 150–152 (1989).
7. X. Yu, A. Todi, and H. Tang, "Bessel beam generation using a segmented deformable mirror," Appl. Opt. **57**, 4677–4682 (2018).
8. R. Bowman, N. Muller, X. Zambrana-Puyalto, *et al.*, "Efficient generation of Bessel beam arrays by means of an SLM," Eur. Phys. J. Spec. Top. **199**, 159–166 (2011).
9. M. Duocastella and C. Arnold, "Bessel and annular beams for materials processing," Laser Photon. Rev. **6**, 607–621 (2012).
10. C. Vetter, R. Steinkopf, K. Bergner, *et al.*, "Realization of free-space long-distance self-healing Bessel beams," Laser Photon. Rev. **13**, 1900103 (2019).
11. L. Stoyanov, M. Zhekova, A. Stefanov, *et al.*, "Zeroth- and first-order long range non-diffracting Gauss-Bessel beams generated by annihilating multiple-charged optical vortices," Sci. Rep. **10**, 21981 (2020).
12. L. Stoyanov, M. Zhekova, A. Stefanov, *et al.*, "Generation of long range low-divergent Gauss-Bessel beams by annihilating optical vortices," Opt. Commun. **480**, 126510 (2021).
13. L. Stoyanov, Y. Zhang, A. Dreischuh, *et al.*, "Long-range quasi-non-diffracting Gauss-Bessel beams in a few-cycle laser field," Opt. Express **29**, 10997–11008 (2021).
14. J. F. Nye and M. V. Berry, "Dislocations in wave trains," Proc. R. Soc. London A **336**, 165–190 (1974).
15. I. Basistiy, V. Bazhenov, M. Soskin, *et al.*, "Optics of light beams with screw dislocations," Opt. Commun. **103**, 422–428 (1993).
16. A. Dreischuh, G. G. Paulus, F. Zacher, *et al.*, "Modulational instability of multiple-charged optical vortex solitons under saturation of the nonlinearity," Phys. Rev. E **60**, 7518–7524 (1999).
17. S. S. R. Oemrawsingh, J. A. W. van Houwelingen, E. R. Eliel, *et al.*, "Production and characterization of spiral phase plates for optical wavelengths," Appl. Opt. **43**, 688–694 (2004).
18. T. Watanabe, M. Fujii, Y. Watanabe, *et al.*, "Generation of a doughnut-shaped beam using a spiral phase plate," Rev. Sci. Instrum. **75**, 5131–5135 (2004).
19. G. Maleshkov, P. Hansinger, N. Dimitrov, *et al.*, "Branching optical signals by fractional vortex dipoles," Opt. Commun. **285**, 3529–3534 (2012).
20. P. Hansinger, G. Maleshkov, N. Gorunski, *et al.*, "Interaction between one-dimensional dark spatial solitons and semi-infinite dark stripes," Opt. Commun. **313**, 106–112 (2014).
21. L. Stoyanov, S. Topuzoski, G. G. Paulus, *et al.*, "Optical vortices in brief: introduction for experimentalists," Eur. Phys. J. Plus **138**, 702 (2023).
22. J. Grover and A. Swartzlander, "Achromatic optical vortex lens," Opt. Lett. **31**, 2042–2044 (2006).
23. C. Mathematical Society of Japan andK. Itô, *Encyclopedic Dictionary of Mathematics*, 2nd ed. (MIT, 1993).
24. N. Mphuthi, L. Gailele, I. Litvin, *et al.*, "Free-space optical communication link with shape-invariant orbital angular momentum Bessel beams," Appl. Opt. **58**, 4258–4264 (2019).
25. A. S. Rao, "A conceptual review on Bessel beams," Phys. Scripta **99**, 062007 (2024).